Characteristics of Correlation Statistics between Droplet Radius and Optical Thickness of Warm Clouds Simulated by a Three-Dimensional Regional-Scale Spectral Bin Microphysics Cloud Model

YOUSUKE SATO,* KENTAROH SUZUKI,[+,#] TAKAMICHI IGUCHI,[@] IN-JIN CHOI,[&] HIROYUKI KADOWAKI, AND TERUYUKI NAKAJIMA**

* *Atmosphere and Ocean Research Institute, The University of Tokyo, Kashiwa, Chiba, and Japan Society for the Promotion of Science, Chiyoda-ku, Tokyo, Japan*
[+] *Department of Atmospheric Science, Colorado State University, Fort Collins, Colorado*
[@] *Earth System Science Interdisciplinary Center, University of Maryland, College Park, and Laboratory for Atmosphere, NASA Goddard Space Flight Center, Greenbelt, Maryland*
[&] *School of Earth and Environmental Sciences, Seoul National University, Gwanak-gu, Seoul, South Korea*
** *Atmosphere and Ocean Research Institute, The University of Tokyo, Kashiwa, Chiba, Japan*

(Manuscript received 11 March 2011, in final form 25 September 2011)

ABSTRACT

Three-dimensional downscaling simulations using a spectral bin microphysics (SBM) model were conducted to investigate the effects of aerosol amount and dynamical stabilities of the atmosphere on the correlation statistics between cloud droplet effective radius (RE) and cloud optical thickness (COT) of warm clouds off the coast of California. The regeneration process of aerosols was implemented into the SBM and was found to be necessary for simulating the satellite-observed microphysical properties of warm clouds by the SBM model used in this study.

The results showed that the aerosol amount changed the correlation statistics in a way that changes the cloud particle number concentration, whereas the inversion height of the boundary layer, which is related to the atmospheric stability and the cloud-top height, changed the correlation statistics in a way that changes the liquid water path. These results showed that the dominant mechanisms that control the correlation statistics are similar to those suggested by previous modeling studies based on two-dimensional idealized simulations. On the other hand, the present three-dimensional modeling was also able to simulate some realistic patterns of the correlation statistics, namely, mixtures of characteristic patterns and the "high-heeled" pattern as observed by satellite remote sensing.

1. Introduction

The climatic effect of clouds is one of the major sources of uncertainties in understanding and predicting global climate change (Stephens 2005). Warm (liquid) clouds, among others, exert particular influence on the radiation budget and hydrological cycle in the earth's climate. Their effect on radiation is characterized by their optical properties, which are typically represented by the cloud droplet effective radius (RE or r_e) and the cloud optical thickness (COT or τ). The COT is the total columnar extinction cross section of cloud particles and is the key parameter in determining cloud reflectivity to solar radiation. The RE is the area-weighted mean radius of cloud droplets and determines the cloud reflectivity in the shortwave infrared spectral windows. The set of the parameters can be retrieved from spectral radiances reflected from the cloud layer (Nakajima and King 1990), and previous remote sensing studies have observed RE and COT from satellites (e.g., Nakajima and Nakajima 1995, hereafter NN95; Han et al. 1994; Kawamoto et al. 2001; Sekiguchi et al. 2003; Myhre et al. 2007; Quaas et al. 2008) and from aircraft (e.g., Nakajima et al. 1991; Brenguier et al. 2000, 2003).

These past remote sensing studies have reported characteristic relationships between COT and RE. Nakajima

[#] Current affiliation: Jet Production Laboratory, California Institute of Technology, Pasadena, California.

Corresponding author address: Yousuke Sato, Atmosphere and Ocean Research Institute, The University of Tokyo, 5-1-5 Kashiwanoha, Kashiwa, Chiba 2778568, Japan.
E-mail: satoy@aori.u-tokyo.ac.jp

DOI: 10.1175/JAS-D-11-076.1

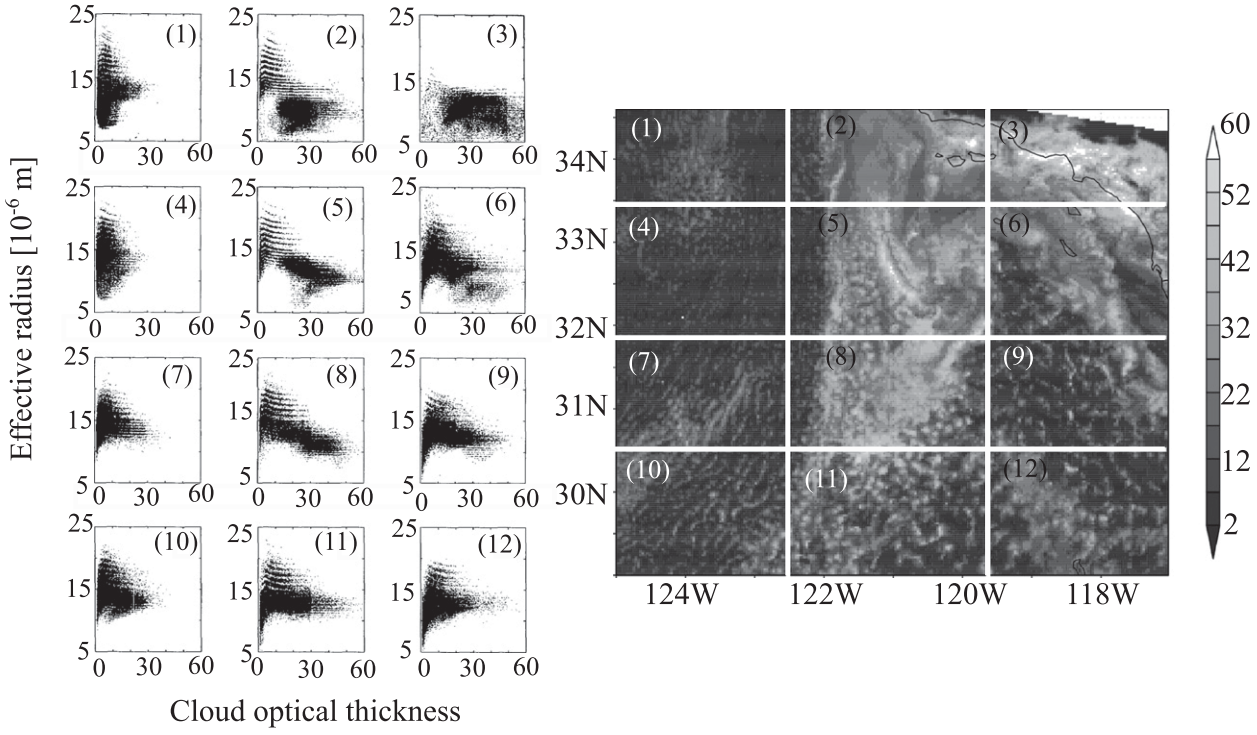

FIG. 1. Scatterplot of (left) cloud effective radius vs cloud optical thickness observed in the FIRE region by NN95 (original figures cited from NN95) and (right) geophysical distribution of cloud optical thickness. The numbers in parentheses in the left panel indicate the domain number in the right panel, from which scatterplots were obtained.

et al. (1991) found that RE and COT tend to be positively correlated when the clouds do not include drizzle-sized particles, whereas they tend to be negatively correlated when the clouds include drizzle-sized particles of a significant concentration. These correlation patterns can be interpreted as a manifestation of the growth processes of cloud droplets that take place in the cloud system. NN95 extended the analysis of Nakajima et al. (1991) into wider regions of the First International Satellite Cloud Climatology Project (ISCCP) Regional Experiment (FIRE) (Albrecht et al. 1988), using Advanced Very High Resolution Radiometer (AVHRR) data, and investigated statistical relationships between RE and COT. Figure 1 presents correlation statistics between RE and COT and the geographical distribution of COT in the FIRE region (cited from NN95 and rearranged for this paper). The figure shows that various relationships can be found between RE and COT, although negative correlation patterns tend to be a dominant relationship. The large portion of the negative correlation branch in most of the panels is often accompanied by a small fraction of positive correlation branches underneath, showing a general ''high-heeled'' shape as argued by Suzuki et al. (2010b). The relationships between RE and COT have also been observationally studied by many investigators (e.g., Asano et al. 1995; Han et al. 1998; Bores and Rotstayn 2001; Kobayashi and Masuda 2008; Lebsock et al. 2008), who also reported that positive and negative correlation patterns tend to occur in a complicated manner depending on the cloud environment. These observational results suggest that the characteristic patterns in the correlation statistics are governed by complicated but ubiquitous microphysical mechanisms involved in the clouds over various regions of the globe.

It is therefore important to understand why these relationships occur in terms of various microphysical particle growth processes. An important key to such an understanding is recent satellite observations that indicate that the microphysical properties of warm clouds are significantly affected by aerosols and static stability of the atmosphere (e.g., Nakajima et al. 2001; Breon et al. 2003; Masunaga et al. 2002; Matsui et al. 2004). For investigating how such environmental factors affect the cloud properties, numerical models are useful tools that also help exploring the detailed formation mechanisms of RE–COT correlations. Recent modeling studies have indeed demonstrated how the aerosol and dynamics affect the clouds and their formation of precipitation (e.g., Khain et al. 2000, 2005; Tao et al. 2007; Iguchi et al. 2008; Choi et al. 2010) although they have not focused on the RE–COT relationships. In this

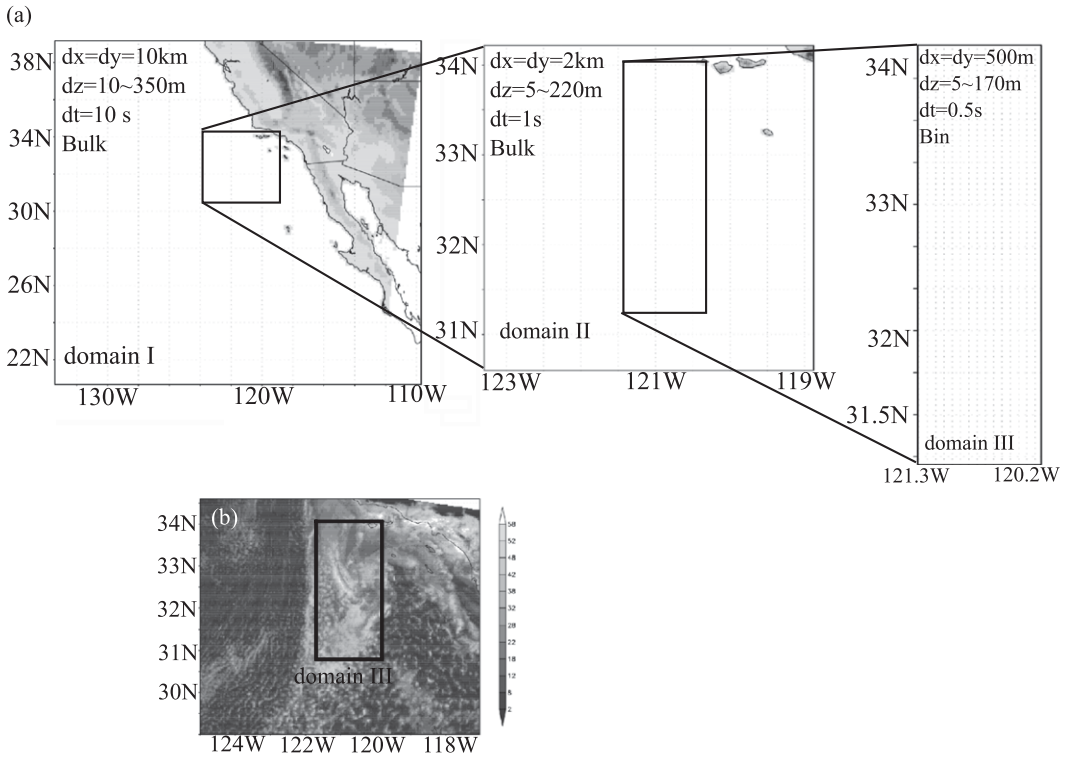

FIG. 2. (a) Domains for multidownscale simulation with *dx*, *dy*, *dz*, and *dt* representing the horizontal and vertical grid spacings and time step. ''Bin'' and ''Bulk'' indicate the microphysical scheme used for the simulation in each domain. (b) Optical thickness observed by satellite in the FIRE region with a black rectangle corresponding to domain III in Fig. 2a.

regard, it is worth noting that Brenguier et al. (2003) investigated RE–COT relationships from aircraft observation and found differences of mean droplet volume radius, which is closely related to RE, calculated over the whole droplet spectrum and that calculated only over the cloud droplets spectrum (i.e., excluding drizzle). However, the observations were limited in narrow area. Lohmann et al. (2000), using a general circulation model (GCM), found the positive and negative correlation patterns between RE and COT for nonprecipitating and precipitating clouds, respectively, offering a hint at possible links between the RE–COT correlation statistics and precipitation processes. Their GCM-based study, however, is not suitable for detailed

TABLE 1. Catalog of the numerical experiment; BULK means bulk microphysical model (Yamada 2003), BIN means spectral bin microphysical model (Khain et al. 2000; HUCM), and SPR means aerosol field nested from SPRINTARS (Takemura et al. 2005). NHM10, NHM2, and NHM500 indicate experiments with 10-km, 2-km, and 500-m grid spacing, respectively. NHM means the dynamical framework (Saito et al. 2006), and X means the experiment did not implement the process.

	NHM10 (domain I)	NHM2 (domain II)	NHM500 (domain III)
Dynamics	NHM	NHM	NHM
Microphysics	BULK	BULK	BIN
Aerosol	X	X	SPR
Horizontal grid spacing	10 km	2 km	500 m
Domain size (horizontal)	2020 km × 2020 km	202 km × 202 km	125 km × 300 km
Vertical grid spacing	10–350 m	5–220 m	5–60 m
Vertical grid number	60	80	60
Model top height	10 160 m	9880 m	1915 m
Initial and boundary condition	JRA	NHM10	NHM2
Calculation time (*dt*)	168 h (10 s)	18 h (1 s)	6 h (0.5 s)
Sampling interval of nesting	6 h	3 h	1 h
Start time	1800 UTC 26 June	1800 UTC 8 July	1000 UTC 10 July

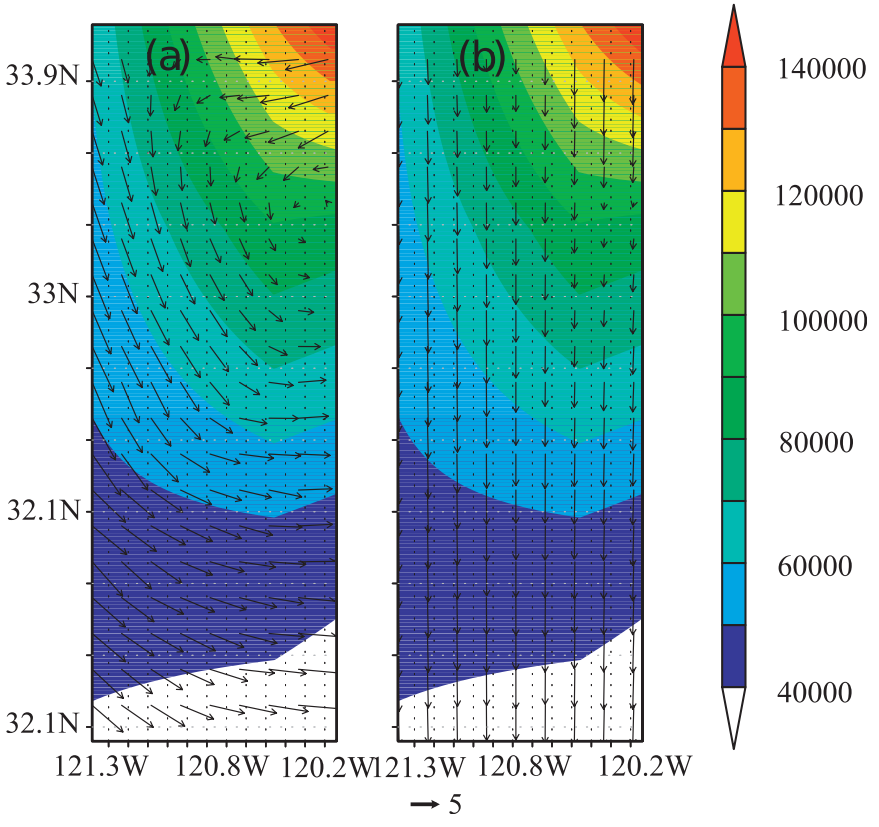

FIG. 3. Column number concentration of aerosol (cm^{-2}, shaded) and horizontal wind velocity ($m\ s^{-1}$) at 600-m height (vector) at the initial time of the domain III calculation in the (a) Na3 and (b) Na3+W experiments.

investigations of cloud microphysical mechanisms since GCMs are based on much coarser grid spacing than the scale of typical individual clouds and are also contingent on highly parameterized representations of cloud microphysical processes.

More recently, a series of studies (Suzuki et al. 2006, 2010a,b) have employed a spectral bin microphysics (SBM) cloud model that predicts explicit changes in the size distribution functions (SDFs) of cloud droplet and have explored formation mechanisms to control the COT and RE relation. These model studies presented successful simulations of the positive and negative correlation patterns of the RE–COT relation for nondrizzling and drizzling clouds, respectively, in a manner consistent with previous observational statistics. They then demonstrated that the static stability and aerosol amount systematically modify the RE–COT statistics through changes in the liquid water path W and the cloud droplet number concentration N_c, respectively (Suzuki et al. 2010a). The shape of the aerosol size distribution function was also found to systematically control the RE–COT correlation pattern (Suzuki et al. 2010b). Their simulations with different aerosol size spectrum slopes showed striking differences in the shapes of the RE–COT correlation patterns that closely resembled those observed over the FIRE and Atlantic Stratocumulus Transition Experiment (ASTEX) (Albrecht et al. 1995) regions as reported by NN95. Suzuki et al. (2010b) found that the correlation patterns became more like the high-heeled shape as illustrated in many panels of Fig. 1 (e.g., domains 5, 7, 8, 9, and 11 in Fig. 1) when the negative slope of the aerosol size spectrum is assumed to be large.

In spite of these novel findings, more studies of the RE–COT relation are required to corroborate the findings of Suzuki et al. (2010a,b), which considered only an isolated cloud in an idealized two-dimensional numerical simulation framework; in particular, more realistic simulations by three-dimensional (3D) models are necessary to confirm the interpretations by these studies and also to investigate how their findings may be applied to understanding of the behavior of clouds formed in the real atmosphere. Recent progress in cloud modeling has enabled us to perform 3D simulations of cloud formation for various purposes. Wang and Feingold (2009a,b) represented a warm cloud structure in 3D idealized

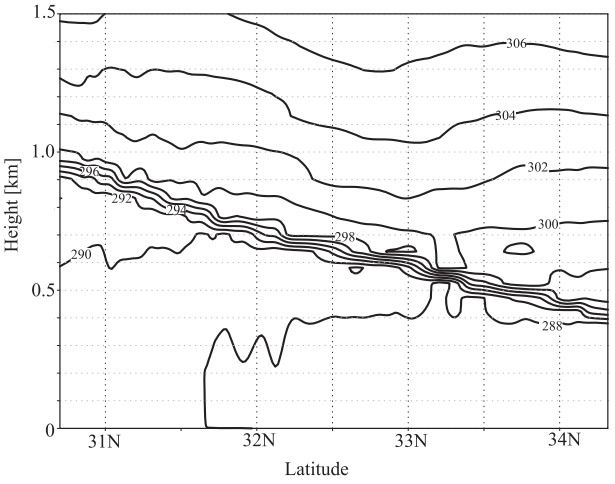

FIG. 4. Latitude–height cross section (longitude = 121°W) of potential temperature (K) at 1500 UTC 10 Jul 1987 calculated by domain II simulation.

simulations assuming the conditions of the Second Dynamics and Chemistry of Marine Stratocumulus field study (DYCOMS-II) (Stevens et al. 2003) using a bin-based bulk microphysical model. Xue et al. (2008) also represented warm clouds by a 3D idealized simulation using SBM. These studies suggested that aerosol amount possibly determines the structure of warm clouds, whereas Wang et al. (2010) indicated that dynamical parameters (e.g., the moisture and temperature perturbations) can also trigger the changes in the structure of warm clouds. All of these studies were nevertheless idealized simulations. Many previous studies were confined to much smaller domains and horizontal resolutions of several meters to several hundred meters (e.g., Ackermann et al. 2009; Stevens et al. 2005; Savic-Jovcic and Stevens 2008; Wang and Feingold 2009a; Feingold et al. 2010; Wang et al. 2011; Mechem et al. 2006; Wang et al. 1993; Mechem and Kogan 2003). Although these studies are useful to understand behaviors and processes for smaller-scale clouds, it is also necessary to perform simulations of wider regions, taking into account the effect of larger-scale environmental conditions and the boundary condition. Previous studies conducted mesoscale simulations of cloudy boundary layers by bulk microphysical model (e.g., Mocko and Cotton 1995). McCaa and Bretherton (2004) investigated impacts of physical parameterizations on cloud-topped marine boundary layers by using the fifth-generation Pennsylvania State University–National Center for Atmospheric Research (NCAR) Mesoscale Model (MM5), and found that the parameterizations can make large impacts. Ivanova and Leighton (2008) investigated the effects of cloud–aerosol interaction on aerosol size distributions by mesoscale model with a double-moment microphysical scheme in the Great Lakes area. Although these studies are very useful to understand the effect of larger-scale environmental conditions and the boundary condition, SBM is more useful because both COT and RE are closely related to the SDFs of clouds. Only one study with 3D realistic simulation, to our knowledge, was done by Iguchi et al. (2008), who developed a 3D SBM model based on a weather forecasting model and conducted a successful nesting simulation to represent a frontal system near Japan with 2- and 7-km grid resolutions with a relatively wide region of 500 km × 500 km horizontal widths.

TABLE 2. Cloud-top height, which is almost the same as the inversion height, at 31.5°N, 121°W observed by FIRE aircraft observations (1717–1722 UTC flight) and calculated by the model in the H0, H+300, and H+500 experiments.

Aircraft observation	Cloud-top height (m)
	~1000
H0	~700
H+300	~1000
H+500	~1200

In this study, real-time 3D downscaling simulations targeting the FIRE region were conducted using a regional SBM to investigate how the cloud microphysical process control the RE–COT statistics as reported in previous studies. This research thus intends to provide a follow-up of the previous studies of Iguchi et al. (2008) and Suzuki et al. (2006, 2010a,b) and to step further by performing a real-time 3D simulation. The objectives of this study are then (i) to reproduce correlation patterns using a 3D-SBM, (ii) to investigate how correlation patterns are affected by environmental conditions (i.e., aerosol effect and dynamical stability), and (iii) to identify the differences between the correlation statistics obtained from the 3D model and those from previous studies based on 2D models and satellite observations. Section 2 describes the model and the experimental setup. Section 3 provides the simulated results, and section 4 discusses the results. The conclusions are summarized in section 5.

2. Model description and experimental setup

a. Model description

Downscaling simulations were conducted for three nested domains over a region off the coast of California (Fig. 2a) on 10 July 1987 when the FIRE field campaign was conducted (Albrecht et al. 1988). The settings of simulations (i.e., domain size, resolution, etc.) are summarized in Table 1 and Fig. 2. The largest, intermediate, and smallest domains are referred to as domains I, II, and III, respectively. Only domain III is analyzed in this paper.

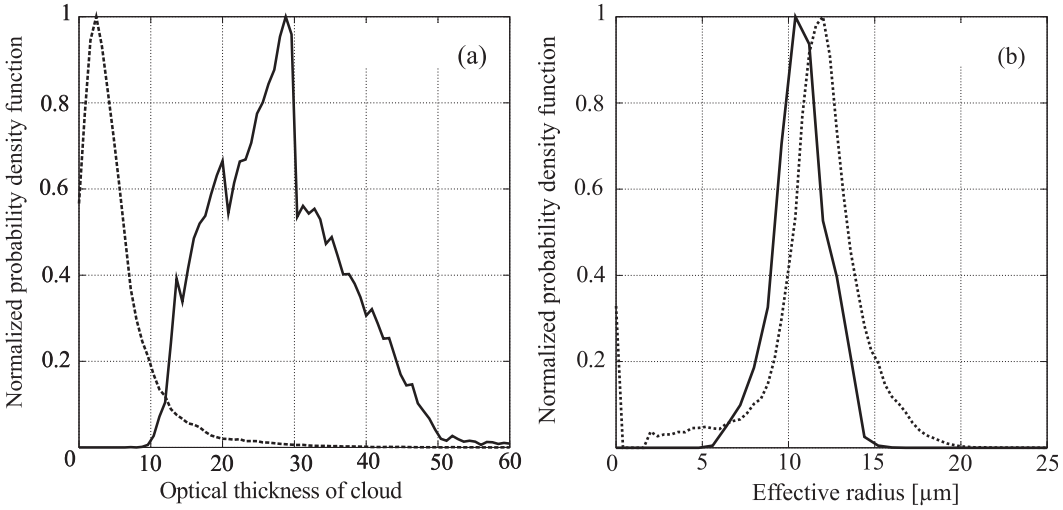

FIG. 5. Normalized PDF of (a) optical thickness and (b) effective radius obtained from satellite observation by NN95 (solid line) and from the control (Na1/H0) simulation (dotted line).

For domain I, data from the 25-yr Japanese Reanalysis Project (JRA-25) (Onogi et al. 2007) were used for the initialization and lateral boundary conditions of dynamical variables, such as horizontal wind velocities, potential temperature, mixing ratio of water vapor, and sea surface temperature (SST). The JRA-25 data have horizontal grid intervals of 2.5°, with 23 vertical layers sampled 4 times per day (i.e., sampled every 6 h). The geographic data were based on the Global 30 Arc Second Elevation Dataset with 1 km resolution (GTOPO30).

The main framework of the mesoscale model is a 3D nonhydrostatic model developed by the Japan Meteorological Agency (JMA-NHM) (Saito et al. 2006) coupled with two types of cloud microphysics modules that are chosen according to the domains. One is a single-moment bulk microphysics module for domains I and II (Lin et al. 1983; Ikawa and Saito 1991; Yamada 2003); the other is a spectral bin microphysics module (for domain III) that consists of a modified version of the Hebrew University Cloud Model (HUCM) (e.g., Khain et al. 2000) for the JMA-NHM and newly developed cloud and aerosol processes (Iguchi et al. 2008; Sato et al. 2009; Choi et al. 2010; this study). Hereafter we refer to this spectral bin microphysics model as UT-ACBM (for University of Tokyo Aerosol–Cloud Spectral Bin Model).

We show a supplementary explanation of the microphysics module of the model for domain III although a detailed description can be found in above-mentioned literature. Only the liquid phase process was calculated in this study because the cloud-top temperature over the region on the date was around 280–290 K, as judged from the reanalysis data, which is much higher than the freezing level. The liquid microphysics includes calculations of nucleation from aerosol particles, condensation/evaporation, and collision–coagulation. The SDF of water droplets are represented on each spatial grid by 33 doubling mass bins that cover particle radii ranging from 2 to 3251 μm. In addition, the SDF of aerosol particles is also discretized into 17 bins as prognostic variables. The chemical composition of particles is assumed to be ammonium sulfate. All aerosols of sizes larger than critical radii are transferred from the aerosol bins to the smallest bin of cloud droplet (Suzuki et al. 2006); the critical radius is calculated on the basis of Köhler theory (Rogers and Yau 1989) using supersaturation and temperature on each grid at every time step. The simulation does not employ a subgrid-scale activation scheme. The subgrid-scale activation can make effects on cloud microphysical properties, and the assumption that all activated clouds are transferred to smallest bin of cloud droplet is very coarse treatment, so we need to improve the scheme in future. The aerosols field for domain III was given from a global simulation by the Spectral Radiation Transport Model for Aerosol Species (SPRINTARS) (Takemura et al. 2005) nested directly to the domain to construct the initial and lateral boundary conditions; the number concentrations of five types of aerosols by SPRINTARS are unified to a binned SDF using a method considering the different water uptake efficiencies of aerosols as cloud condensation nuclei (CCN) (Iguchi et al. 2008; Choi et al. 2010).

A regeneration process of aerosols from completely evaporated droplets was newly implemented into the spectral-bin microphysical framework following the method of Feingold et al. (1996). This parameterization assumes that complete evaporation of a cloud particle

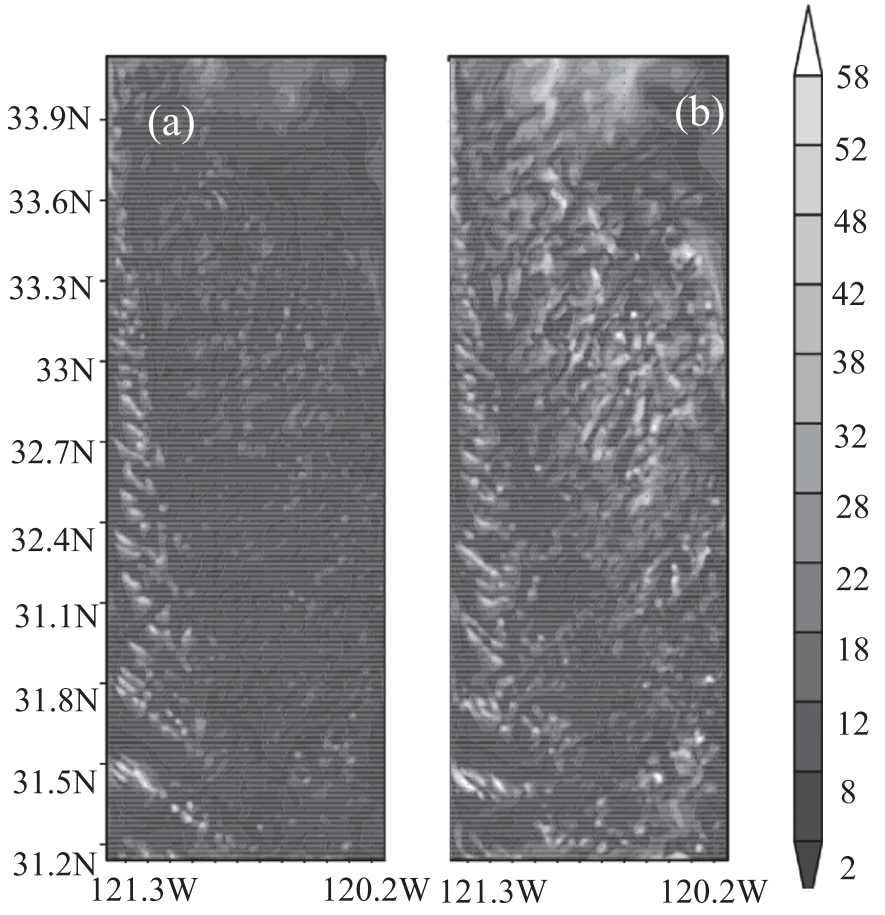

FIG. 6. Cloud optical thickness at 1500 UTC 10 Jul 1987 simulated by the model (a) without and (b) with regeneration.

generates one aerosol particle based on Mitra et al. (1992). And the size distribution of regenerated aerosols is determined by the domain-averaged number of aerosols at initial time and each time step (Feingold et al. 1996). As well as this regeneration, we calculated nucleation, condensation/evaporation, and collision–coagulation processes at each time step and spatial grid by the microphysical scheme of our model. For the collision and coagulation processes, we implemented a scheme based on the Monte Carlo method (Sato et al. 2009) to reduce computational costs. The radiation scheme is MXTRN-X developed by Nakajima et al. (2000) and Sekiguchi and Nakajima (2008). The radiation scheme also calculated longwave radiation flux.

b. Sensitivity experiments

Several sensitivity experiments were performed in order to understand the cloud behavior simulated in the FIRE region. First, sensitivity experiments with and without the aerosol regeneration process were performed to underscore the importance of the process to reproduce realistic cloud fields.

Second, sensitivity experiments that changed the aerosol amount were performed to investigate the effects of aerosol amount as studied by Suzuki et al. (2006, 2010a). The initial condition of the SDF for aerosols in domain III is given as

$$f_a(r_a) = \sum_{i=1}^{N_m} \frac{N_{\mathrm{spr}} A_i}{\sqrt{2\pi}\sigma_i} \exp\left(-\frac{\ln r_a - \ln r_{0i}}{2\sigma_i^2}\right), \qquad (1)$$

where f_a and r_a are number concentration and radius of the aerosol particle, respectively. Also, N_m is the number of modes of SDF, and A_i, r_{0i}, and σ_i are the mode fraction, mode radii, and geometrical standard deviation [see Choi et al. (2010) for details of A_i, r_{0i}, N_m, and σ_i], and N_{spr} is the number concentration computed by SPRINTARS. The horizontal distribution of column accumulated N_{spr} is shown as shaded in Figs. 3a and 3b. We then carried out two sensitivity experiments, called

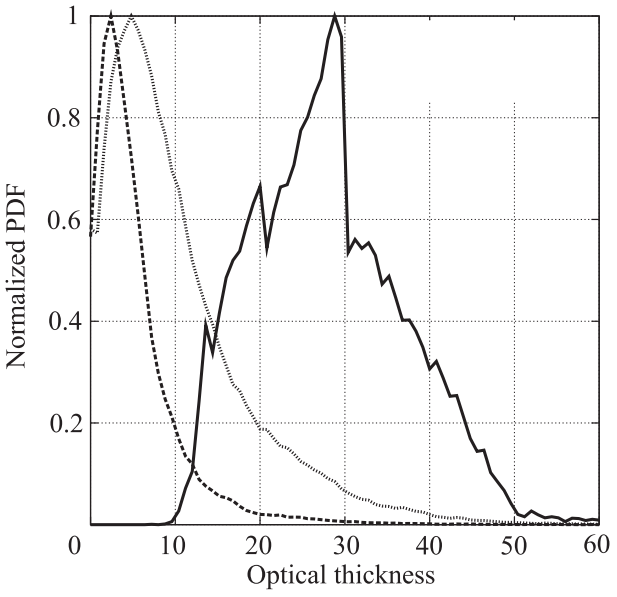

FIG. 7. Normalized PDF of optical thickness obtained from satellite observation by NN95 (solid line) and from model with (dashed line) and without regeneration (dotted line).

the Na3 and Na5 experiments, by changing N_{spr} threefold and fivefold, respectively, from the value in the control run (referred to as the Na1 experiment).

Third, the height of the temperature inversion was changed. The height was defined as the lowest grid where potential temperature was 3 K lower than that of the upper grid. Meridional and vertical profiles of the potential temperature obtained from the domain II calculation are shown in Fig. 4. The inversion height was simulated at 400–900 m over the northern to southern areas of domain II. When nested from domain II to domain III, we performed the two stability change sensitivity experiments named H+300 and H+500 by raising the potential temperature and vapor mixing ratio profiles in the vertical direction by 300 and 500 m, respectively, from the height in the control run (referred to as the H0 experiment). This treatment reduces the potential temperature at the model top and also reduces the potential temperature difference between the model's top height and the surface. The lower tropospheric static stability (LTSS; Klein and Hartmann 1993), defined by the difference in the ground potential temperature from that at 700 hPa, was calculated in the H0 (initial condition), H+300, and H+500 experiments, with extrapolation of the potential temperature to the 700-hPa level. The LTSS values were thus calculated as 30.38, 27.63, and 25.99 K, respectively. It should be noted that the inversion height in the control run (H0 experiment) was lower than that observed by aircraft (Table 2), and that of the H300 experiment was closest to the aircraft observation value.

Finally, we conducted sensitivity experiments that change the horizontal wind direction with the Na3 aerosol condition and the H+300 inversion height to examine the effect of the geographical distribution of aerosols on RE–COT correlation patterns. The initial horizontal wind in this experiment (henceforth referred to as the Na3+W experiment) was given as

$$\begin{cases} u_{\text{na3+W}} = 0 \\ u_{\text{na3+W}} = \sqrt{u_{\text{na3}}^2 + v_{\text{na3}}^2}, \end{cases} \tag{2}$$

where u and v are the zonal and meridional wind speeds, respectively, and the subscripts na3 and na3+W indicate the Na3 and Na3+W experiments, respectively. The geographical distributions of column aerosol amount and wind velocity at the cloud layer (i.e., 600 m) are shown in Fig. 3b.

3. Results

a. State of clouds observed on the analysis day

Before showing the model results, we present the state of clouds observed on the day of analysis to clarify what kind of clouds should be reproduced by the model calculation. At 1500 UTC 10 July 1987, the AVHRR crossed the area off the coast of California. NN95 analyzed these AVHRR data and retrieved the COT and RE as shown in Fig. 1 (left). They suggested that an aerosol flow from the North American continent increased COT in the eastern part of the observed domain. In the western part, which was not affected by the continental aerosol flow, COT was found to be small with large cloud particles. At the same time, aircraft measurements observed the cloud-top height to be about 1000 m (Table 2).

b. General characteristics of clouds simulated by control run

The satellite observation shown above was performed at 1500 UTC 10 July 1987, so we first analyzed the simulated results for domain III at 5 h after the beginning of the domain III simulations (1500 UTC 10 July 1987), which corresponds to the time when the satellite observations were made. Figure 5 compares the probability density function of COT and RE. In the model, COT τ and RE r_e are calculated as

$$\tau = 2\pi \int_{z=0}^{z=z_{\text{top}}} \int_{r=2.1\mu\text{m}}^{r=3251\mu\text{m}} r^2 f_c(r)\, dr\, dz, \tag{3}$$

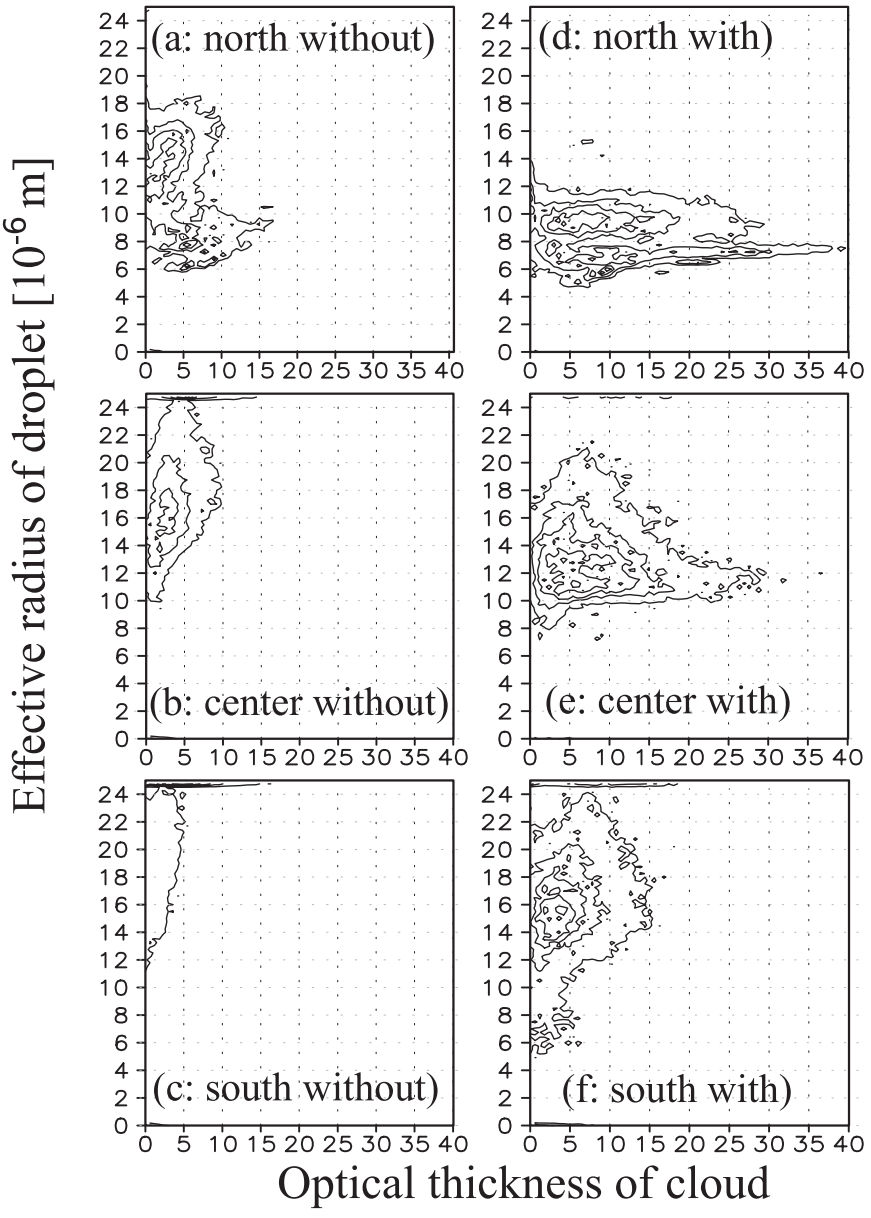

FIG. 8. Normalized correlation pattern between cloud optical thickness and cloud effective radius obtained from the results simulated (a)–(c) without and (d)–(f) with regeneration. Scatterplots are obtained from the (a),(d) northern, (b),(e) central, and (c),(f) southern parts of domain III divided into three parts in the meridional direction. The contours are for 0.1, 0.3, 0.5, 0.7, 0.9, with the maximum value set to 1.

$$r_e = \frac{\int_{r=2.1\mu\mathrm{m}}^{r=3251\mu\mathrm{m}} r^3 f_c(r)\, dr}{\int_{r=2.1\mu\mathrm{m}}^{r=3251\mu\mathrm{m}} r^2 f_c(r)\, dr}, \tag{4}$$

where f_c is the SDF of cloud particles and z_{top} is the model top height. Compared in Fig. 5 are those obtained from the simulation under the Na1 and H0 conditions. From the figure it is found that the model underestimated the observed COT, while it overestimated the observed RE. These results suggest that cloud particles in the model tend to grow more rapidly than those in the real atmosphere and are then likely to fall faster from the cloud layer as precipitation. The model also simulated a cloud-top height lower than observed (Table 2) due to the lower inversion height.

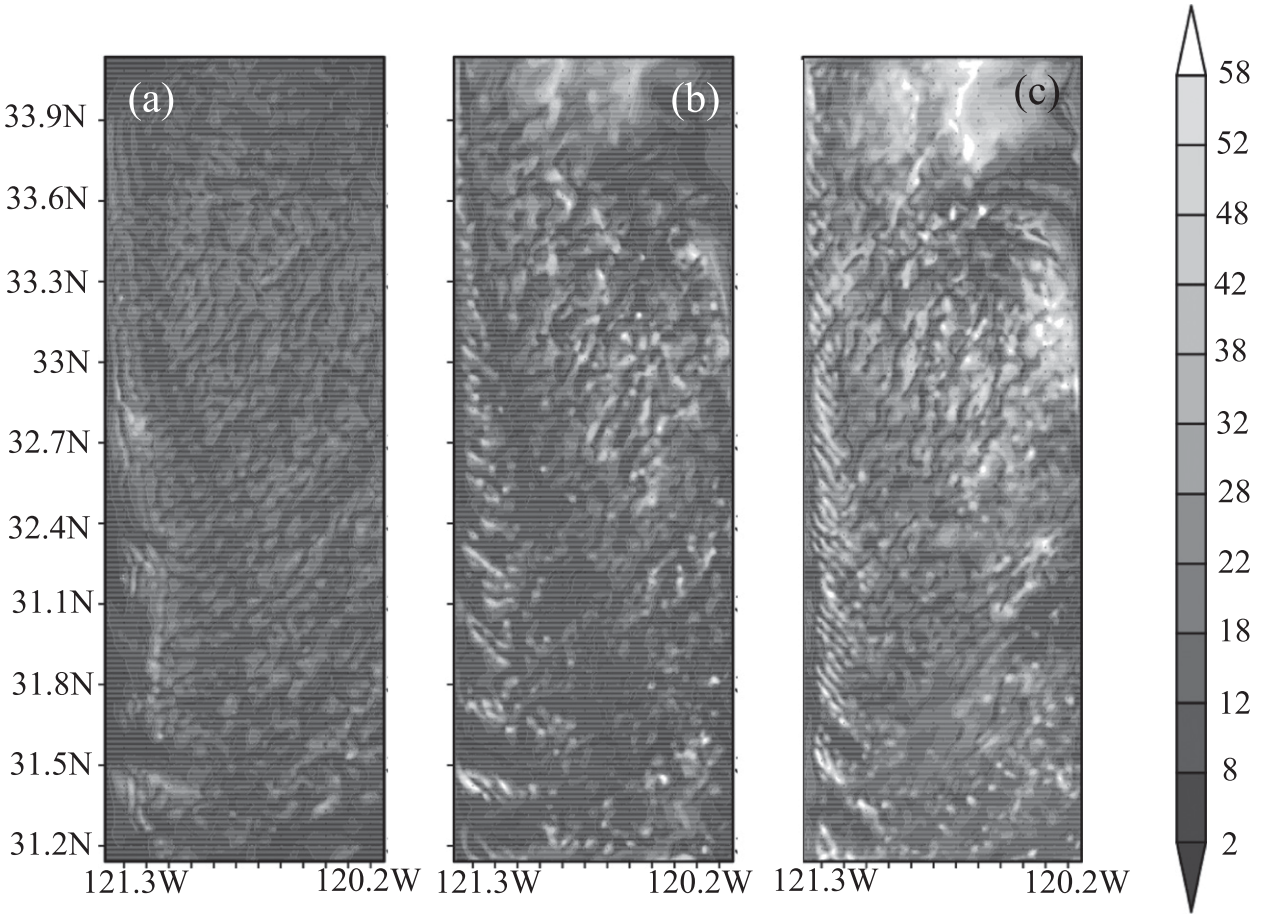

FIG. 9. As in Fig. 6, but obtained from the (a) H0, (b) H+300, and (c) H+500 experiments, respectively.

c. Aerosol regeneration processes

The smaller COT and the larger RE simulated by the model may be attributed to insufficient aerosol amount in the model, where aerosols are only consumed by the nucleation process without any supply. To explore this effect on the cloud formation, sensitivity experiments incorporating the aerosol regeneration process were performed using conditions of Na3 and H+300 that reproduced the inversion height and optical thickness closest to aircraft and satellite observations (Table 2). Figures 6a and 6b show COT at 1500 UTC 10 July obtained from the experiments with and without the aerosol regeneration process, respectively, and Fig. 7 compares the normalized probability distribution functions (PDFs) of COT with satellite-observed PDFs. These figures show that the clouds were simulated optically thin without regeneration, whereas the clouds became optically thicker with regeneration, suggesting that the aerosol supply by cloud particle evaporation is not negligible for the formation process of the target cloud system. The column number concentration of aerosols at 1500 UTC 10 July, averaged over domain III with and without regeneration, are 7.21×10^4 and 5.92×10^4 cm^{-2}, respectively, which indicates that about 20% of aerosols are supplied by regeneration process. However, the PDFs obtained from the simulations show that the model still underestimates the COT even when the regeneration process was implemented.

We next investigated the dependence of the RE–COT correlation statistics on the cloud microphysical characteristics. In this analysis, we produced the RE–COT scatterplots using RE values at a depth from the cloud top corresponding to 30% of the total optical thickness because the RE observed from satellite is the RE at a layer whose cloud optical depth reaches 20%–40% of the COT from cloud top (Nakajima and King 1990). Figure 8 shows the RE–COT correlation statistics for the region corresponding to those observed by NN95 as shown in their Fig. 17 (or our Fig. 1, left). Figures 8a–c (Figs. 8d–f) present the statistics obtained without (with) regeneration. Results with regeneration reproduced the high-heeled form of the correlation statistics in the central part of domain III (Fig. 8e), similar to those observed over the FIRE region by NN95

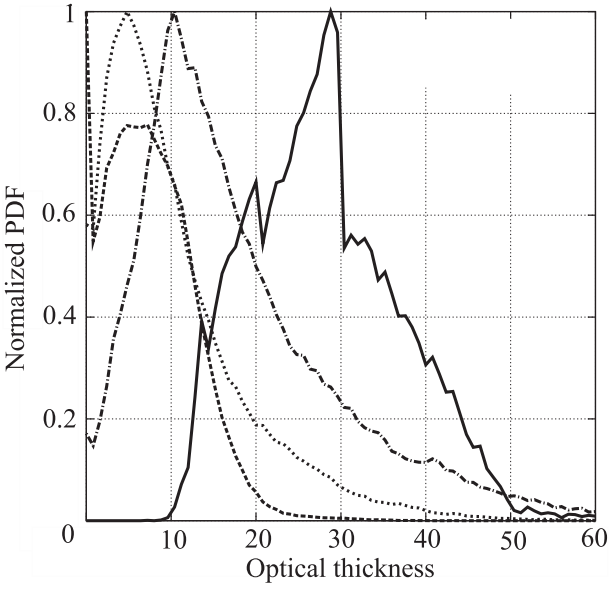

FIG. 10. As in Fig. 7, but obtained by satellite observation (solid line) and calculated by the H0 (dashed line), H+300 (dotted line), and H+500 (dotted–dashed lines) experiments, respectively.

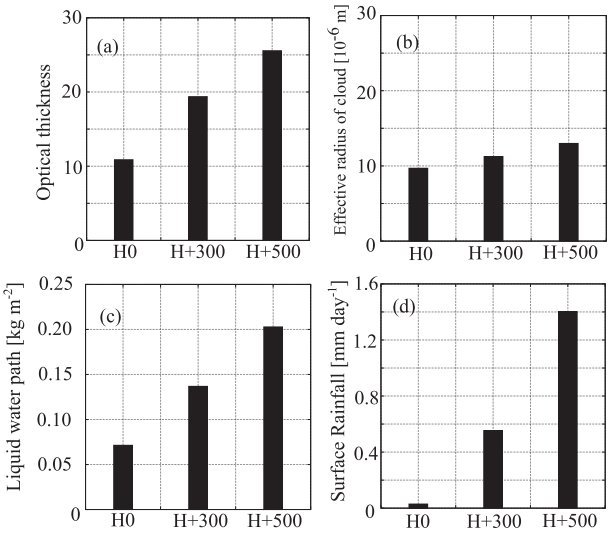

FIG. 11. (a) Cloud optical thickness, (b) effective radius (μm), (c) liquid water path (kg m^{-2}), and (d) surface rainfall (mm day^{-1}) averaged over all cloudy grids in domain III. The effective radius was taken from the layer where optical thickness reached 30% of the whole optical thickness from the top of the clouds.

(e.g., domain II in Fig. 1, left) and also to those simulated by a previous modeling study (Suzuki et al. 2010b). Without regeneration (Figs. 8a–c), almost all the contours concentrate more in the left and upper region of the RE–COT plane compared to those obtained from simulations with regeneration, indicating that the clouds, when lacking the regeneration process, were optically thinner and the particles had grown larger than in the experiment with regeneration. These results suggest that the regeneration process is necessary for the model to simulate warm cloud properties more realistically.

Even with regeneration, however, the comparison of the simulated COT with those observed from satellite (i.e., Fig. 2b) revealed underestimates of COT and large differences in their amount and geographical distribution. These differences probably arose from the uncertainty in meteorological and aerosol fields that were used for initial and lateral boundary conditions of the model. The meteorological fields were derived from JRA-25 data with relatively coarse resolution of 2.5° × 2.5°, and the aerosol fields were from the SPRINTARS global model with a grid spacing of 1.125° × 1.125°, while the model resolutions for domains I, II, and III are 10 km, 2 km, and 500 m, respectively. Future work is also needed to improve the regeneration process for better simulation of CCN distribution.

d. Effect of inversion height

The second sensitivity experiment was conducted by changing the inversion height, which relates to the atmospheric static stability, with prescribed aerosol amounts to investigate how the atmospheric stability affects clouds simulated by the model. The height of the temperature inversion was increased from the control value (H0) to 300 m (H+300) and 500 m (H+500), with the aerosol amount fixed to 3 times as large as the control value (Na3). Figure 9 shows the geographical distributions of COT in domain III obtained from the sensitivity experiment, and Fig. 10 shows the PDFs of COT obtained by satellite observation and simulations. The COT was found to increase monotonically with increasing the inversion height. Shown in Fig. 11 are COT (τ), RE (r_e), LWP (W), and the surface rainfall rate averaged over all cloudy grid columns for the last 4 h of calculation. The LWP was calculated as

$$W = \int_{z=0}^{z=z_{\text{top}}} \int_{r=2.1\mu\text{m}}^{r=3251\mu\text{m}} \frac{4}{3} r^3 \rho_w f_c(r)\, dr\, dz, \qquad (5)$$

where ρ_w is density of water and the cloudy columns are defined as those with COT greater than 0.1. As shown in Fig. 11, clouds that formed under higher inversion heights had larger values of COT, RE, and LWP, and higher surface rain rates. This was due to the fact that clouds can grow geometrically thicker under higher inversion heights.

Although the simulation underestimated the COT as mentioned above, the results are still meaningful to an investigation of the effect of inversion height on RE–COT correlation statistics to find the signatures of particle growth processes. Figure 12 shows the RE–COT correlation

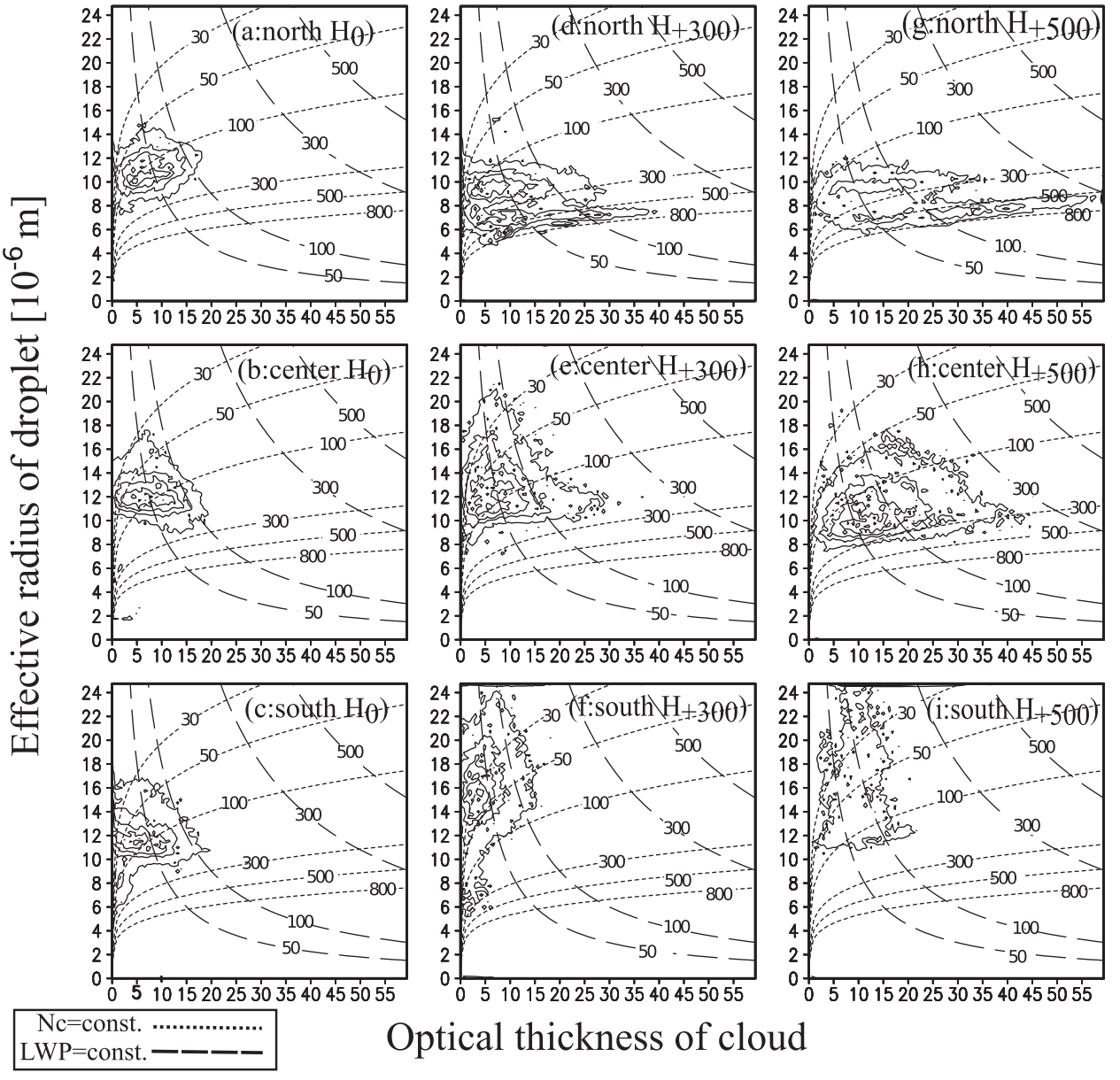

FIG. 12. As in Fig. 8, but obtained from the sensitivity experiment. Results are for the (a)–(c) H0, (d)–(f) H+300, and (g)–(i) H+500 experiments for the (a),(d),(g) northern, (b),(e),(h) central, and (c),(f),(i) southern parts of domain III, respectively. The contours are for 0.01, 0.1, 0.3, 0.5, 0.7, 0.9 for (i) and 0.1, 0.3, 0.5, 0.7, 0.9 for (a)–(h), with the maximum value set to 1. The dotted and dashed curves are isolines of N_c and W, respectively, based on the adiabatic model (Brenguier et al. 2000). The isolines are for N_c = 30, 50, 100, 300, 500, and 800 and W = 50, 100, 300, and 500 g m^{-2}.

statistics as in Fig. 8, obtained from the inversion height sensitivity experiment. The dotted and dashed curves represent isolines for N_c and W provided by the adiabatic model (Brenguier et al. 2000), which are given as

$$\tau = \begin{cases} \dfrac{8}{5}(\pi k)^2 \dfrac{\rho_w}{\lambda} N_c^2 r_e^5(H) & (N_c = \text{const.}) \\ \dfrac{9}{5}\dfrac{1}{\rho_w}\dfrac{W}{r_e} & (W = \text{const.}) \end{cases}, \quad (6)$$

where H is the geometrical height from the cloud base and ρ_w is the density of water (Suzuki et al. 2010a). The parameters k and λ denote coefficients relating the volume-mean radius to the effective radius and the adiabaticity factor, respectively. Values for k and λ were set at $k^{-1/3} = 1.1$ and $\lambda = 5.2 \times 10^{-3}$ g m^{-4}, respectively, following Suzuki et al. (2010b). Although the clouds do not always grow as the adiabatic model predicts, the model, when applied to the complicated SBM results,

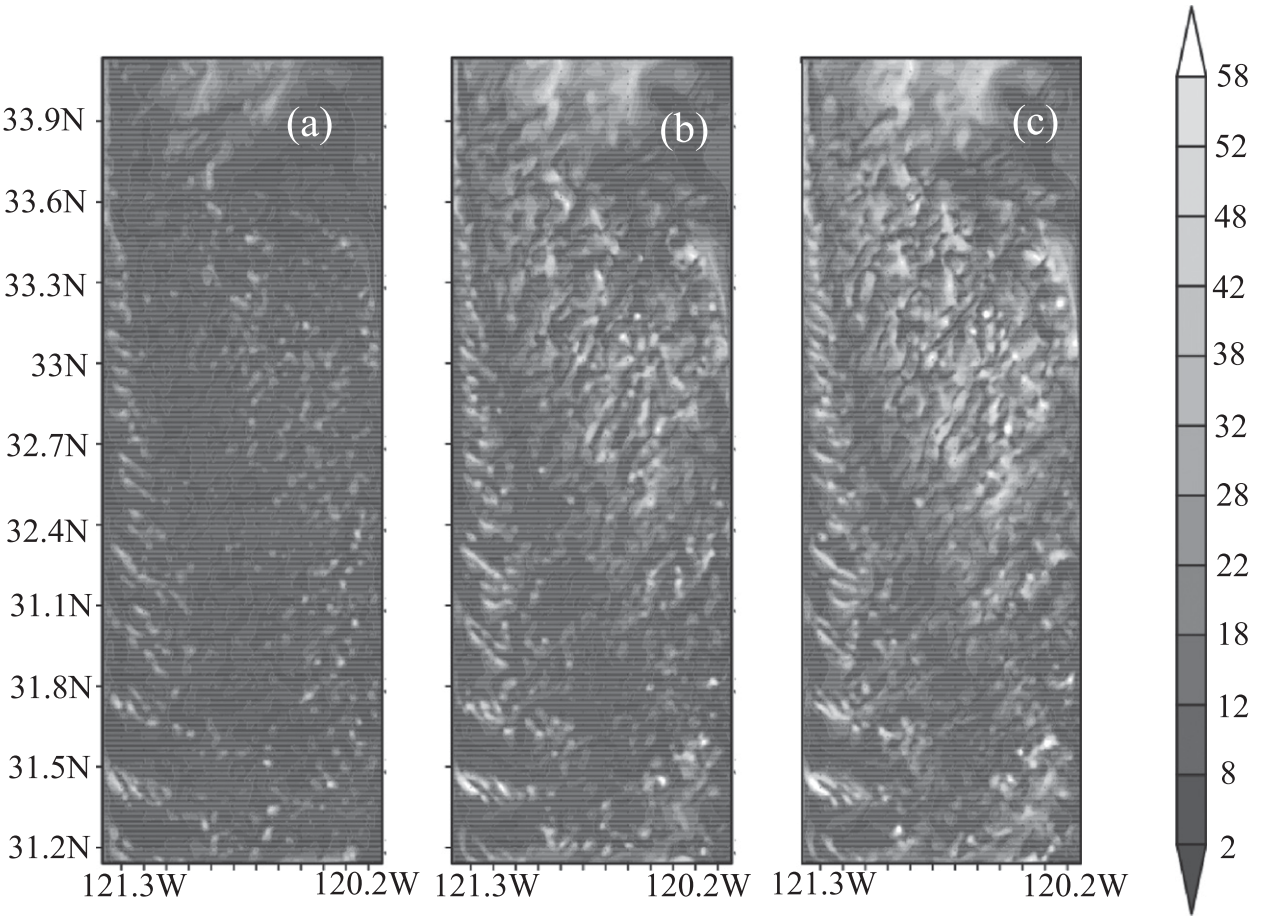

FIG. 13. As in Fig. 9, but obtained with (a) Na1, (b) Na3, and (c) Na5, respectively.

provides a useful theoretical framework that is simple enough to obtain understandings of how the particle growth processes tend to link to fundamental cloud properties such as LWP and N_c. It is nevertheless worth noting that the adiabatic model still has a limitation as will be discussed in section 4.

Suzuki et al. (2010a) proposed that there exist three stages in the cloud life cycle as follows: 1) stage 1, characterized by a positive correlation between RE and COT, 2) stage 2, characterized by a negative correlation, and 3) stage 3, which corresponds to another positive correlation that occurs for small COT and large RE. Suzuki et al. (2010a) then interpreted the condensation, collision, and evaporation processes as being dominant in stages 1, 2, and 3, respectively. In the stage 1, the contours of the RE–COT statistics locate mostly along the isolines of N_c because N_c is constant when the cloud particles grow by the condensation process, whereas the contours are more like along the isolines of W in stage 2, where the mass of hydrometeors tends to be conserved under the dominance of the collision–coalescence process. In stage 3, both the number and mass concentrations do not conserve, being affected by the evaporation process, so that the contours tend to cross both the isolines of N_c and W. In the H+300 (Figs. 12d–f) and H+500 experiments (Figs. 12g–i), the statistics appeared to include positive and negative correlations corresponding to the cloud growth stages suggested by Suzuki et al. (2010a). In the northern part of domain III (Figs. 12d,g), for instance, the lowest edge of the contour closely follows the isoline of $N_c = 800$ cm^{-3}, which appears to correspond to stage 1 dictated by the condensation process for a specified value of $N_c = 800$ cm^{-3}. In the central part of domain III (Figs. 12e,h), in contrast, the upper-right edge of the contours tends to run along the isoline of W for around 200 g m^{-2}, exerting a negative correlation pattern between RE and COT. This appears to indicate stage 2, where the collision–coalescence process dominates the cloud particle growth. In the southern part of domain III (Figs. 12f,i), smaller COT and larger RE were found, suggesting that stage 3, dominated by the evaporation process, is considered to mainly take place. In the

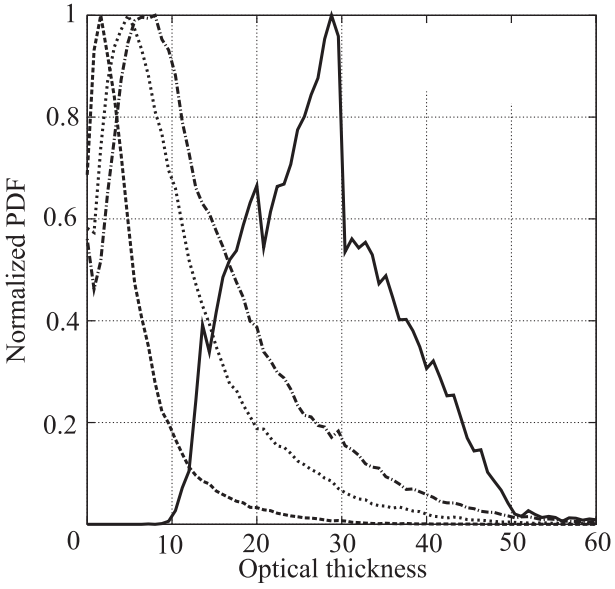

FIG. 14. As in Fig. 10, but obtained from satellite observation (solid line) and calculated by the Na1 (dashed line), Na3 (dotted line), and Na5 (dotted–dashed line) experiments, respectively.

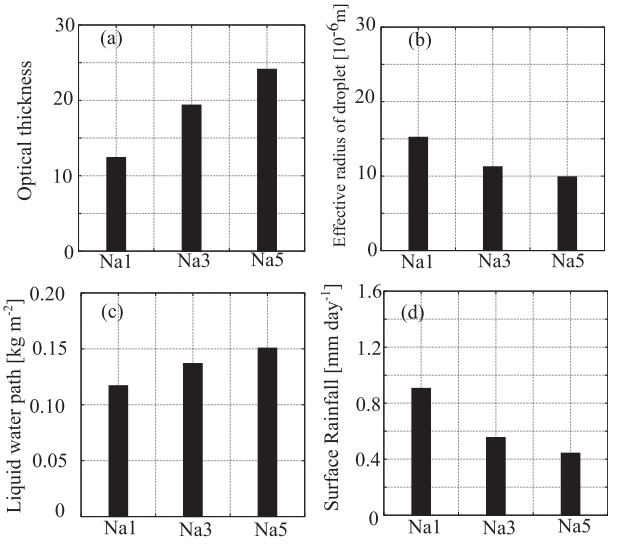

FIG. 15. As in Fig. 11, but obtained from the sensitivity experiment with changing aerosol amount.

H0 experiment, positive and negative correlation patterns were also reproduced, although they were less clear because the clouds grew less on account of the lower inversion height.

In the southern part of the H+500 experiment (Fig. 12i), a large number of contours were concentrated over the region where RE exceeds 25 μm. This means that cloud droplets grow more rapidly for higher inversion height. Except for these contours, Fig. 12 shows that the change in the inversion height clearly affected W. In the central part, W reached about 280 g m^{-2} in H+500 (Fig. 12h), 210 g m^{-2} in H+300 (Fig. 12e), and 120 g m^{-2} in H0 (Fig. 12b). In contrast to the effect of the inversion height on W, its effect on N_c was found to be small.

The abovementioned trends were similar to those reported by Suzuki et al. (2010a). However, the shape of the scatterplots differs from those reported by Suzuki et al. (2010a). In this study, multiple clouds were simulated in the calculation domain, and the RE–COT scatterplot contains various states of the different cloud properties, while Suzuki et al. (2010a) simulated only isolated clouds. The mixture of multiple cloud properties may have made the shapes of the scatterplots more distorted and diffused compared to those produced by Suzuki et al. (2010a). This point will be discussed below in section 4.

e. *Effect of aerosol amount*

The third sensitivity experiment was performed by changing the amount of aerosol to 5 times the control value with an inversion height fixed at the H+300 condition because this inversion height value was the closest to the observed one (Table 2). Figures 13 and 14 show the geographical distributions of COT and the PDF of COT, respectively, obtained from the sensitivity experiment. It is found that larger aerosol amounts resulted in optically thicker clouds. The bar graphs shown in Fig. 15 are the same as those in Fig. 11 but are obtained from the aerosol amount sensitivity experiments. The COT and W increased with increasing aerosol amount, whereas RE and surface rainfall decreased with increasing aerosol amount. These tendencies are those qualitatively expected from the aerosol effects suggested by previous studies (Twomey 1974; Albrecht 1989). However, it is noteworthy that the aerosol-induced changes in COT, W, RE, and the surface rainfall rate are smaller in magnitude than those that occur when the inversion height is changed.

Figure 16 shows the RE–COT correlation statistics obtained by change in the aerosol amount. The positive and negative correlation patterns indicative of different cloud particle growth stages, as discussed above, were also reproduced in all experiments, although they were not clear as in the case of Na1 case. Compared with the isolines for N_c and W given by the adiabatic model, the change in the aerosol amount was found to clearly affect N_c. The larger the aerosol amount was, the higher the N_c became, whereas variations in W were small for the increase in aerosol amount. These trends were also similar to those obtained by satellite remote sensing (Nakajima et al. 2001) and by models (Suzuki et al. 2004, 2010a). The present study, however, produced distorted and diffused patterns (e.g., Figs. 16a,h; bimodal distribution) in the scatterplot. This point will also be discussed in the next section.

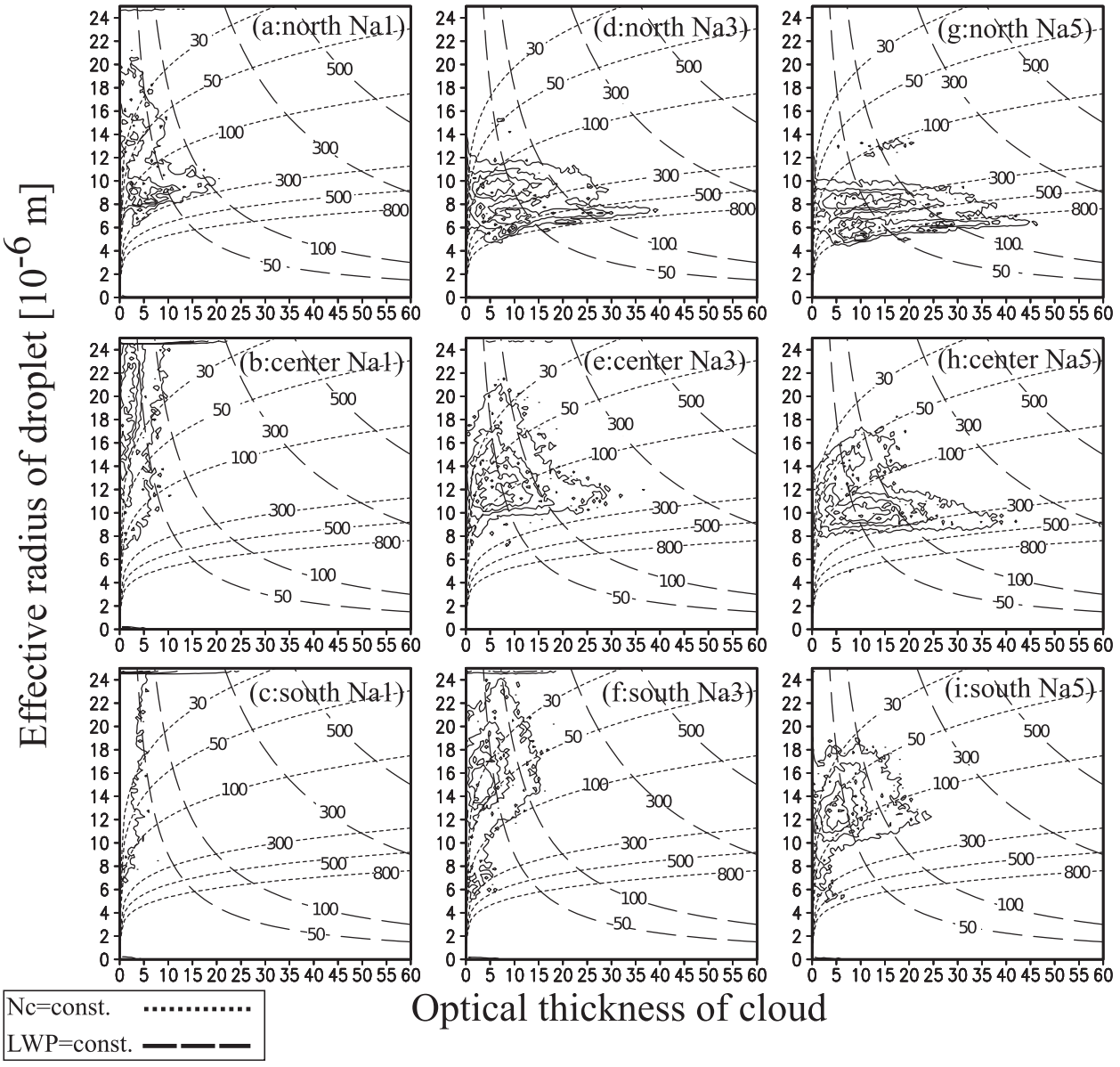

FIG. 16. As in Fig. 12, but obtained from the sensitivity experiment with changing aerosol amount. Results are for the (a)–(c) Na1, (d)–(f) Na3, and (g)–(i) Na5 experiments for the (a),(d),(g) northern, (b),(e),(h) central, and (c),(f),(i) southern parts of domain III, respectively.

Figure 17 summarizes the tendency of changes in the RE–COT correlation statistics obtained from the sensitivity studies. The uppermost edges of the contour move along the isoline of W to cross the N_c isolines as the aerosol amount increases, indicating that an increase in aerosol amount tends to increase N_c with small changes in W values. When the inversion height changes, in contrast, the uppermost edges of the contour move across the W isoline, indicating that the higher the inversion height (the greater the instability) was, the larger the W became. This means that the inversion height changes the water content of cloud droplets with small changes in their number concentration and that the larger inversion height causes large cloud particles, resulting in more rainfall. These characteristic patterns in the correlation statistics will be discussed further in the next section.

4. Discussion

In section 3 we showed that the present 3D model can reproduce the positive and negative correlation patterns

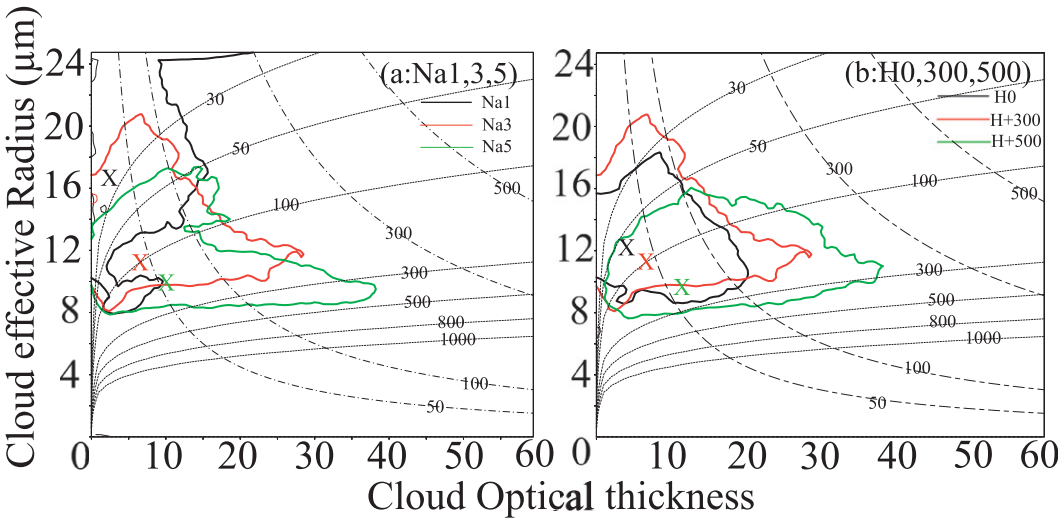

FIG. 17. Summarized correlation pattern obtained from the center of domain III by (a) the changing aerosol amount sensitivity experiment and (b) the changing inversion height sensitivity experiment. The black, red, and green solid lines are the smoothed contours obtained from (a) Na1, Na3, and Na5 and (b) H0, H+300, and H+500, respectively. The contours are 0.05 with the maximum value set to 1. The X indicates the center of each contour.

in the RE–COT statistics as proposed by previous studies (Suzuki et al. 2010a), but the simulated statistics also included other complex patterns as shown in Figs. 12, 16, and 17, which are also found in the satellite-observed statistics (e.g., NN95). This section studies formation mechanisms of such complex RE–COT relations.

a. Bimodal characteristics of the RE–COT scatterplot

A distinctive feature found in the 3D simulations is the bimodal patterns shown in Fig. 16h. The patterns are found to be comprised of two groups divided by the isoline of $N_c = 100$ cm^{-3}. This feature did not appear in the previous studies (Suzuki et al. 2010a,b), even though the cloud microphysical scheme used in previous studies was essentially same as the one used here (i.e., UT-ACBM). The major difference in this study compared to previous studies is multiple clouds instead of an isolated cloud reproduced in more realistic forecast-type simulations. Hence, the bimodal feature must reflect two kinds of clouds with different microphysical properties coexisting in the calculation domain: one with droplet number concentrations greater than about 100 cm^{-3}, and the other with number concentrations less than about 100 cm^{-3}. Figure 18 presents separate geographical distributions of COT for these two kinds of clouds grouped by $N_c = 100$ cm^{-3} (henceforth this threshold value of N_c is referred to as N_t). The figure shows that the clouds corresponding to a lower number concentration (i.e., $N_c < N_t$) were located in the western part of the computational domain and were optically thinner, whereas the clouds corresponding to a greater number concentration (i.e., $N_c > N_t$) were located over the northern and eastern parts of the domain. This geographical distribution of the different kinds of cloud was determined by the distribution of aerosol amount and the wind field at the initial time in the domain III calculation, as shown in Fig. 3a. A high pressure system is located around 37°N, 140°W, which causes an anticlockwise flow, which in turn results in the northwest wind and the aerosol transport from the northern and western boundary of the calculation domain III. This characteristic pattern is to some extent similar to the satellite-retrieved distributions of COT and RE shown in NN95 on 10 July 1987 with a distinct difference in the COT and RE values between western and eastern regions of their observation separated by a longitude of 122°W (Fig. 2b). To further isolate the effect of this inhomogeneous aerosol transport distribution, an additional simulation was conducted using uniform horizontal winds (i.e., the Na3+W experiment; Fig. 3b). This setup generated a polluted air mass for almost all of domain III. The RE–COT statistics obtained from the Na3+W experiment are shown in Fig. 19. It is found from the figure that the scatterplots are composed of a single group, in contrast to the bimodal pattern in Fig. 16h. And the scatterplot for the southern part (Fig. 19b) has the high-heeled form identified by Suzuki et al. (2010b). These results reveal that the bimodal characteristic of the scatterplot is generated from multiple clouds with different microphysical characteristics caused by the inhomogeneity of aerosols in the domain III.

b. Theoretical interpretation of the RE–COT pattern

The analysis in the previous section indicated that the bimodal distribution of RE–COT statistics could be

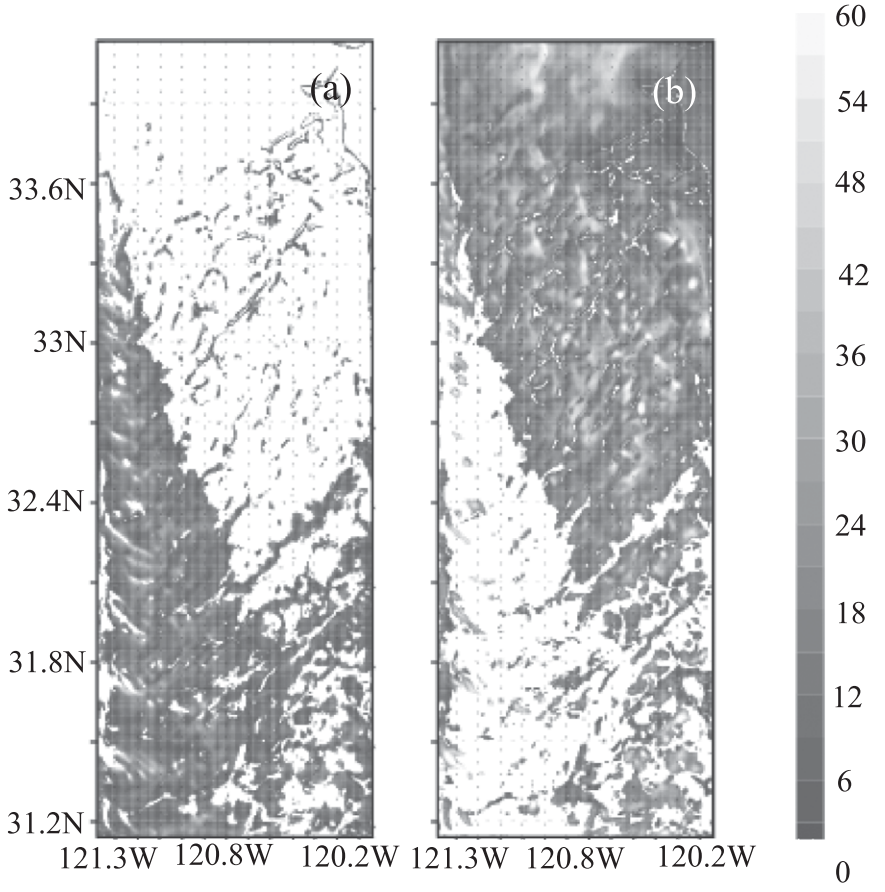

FIG. 18. Optical thickness for regions with number concentration (a) larger and (b) smaller than 100 cm^{-3} at 1500 UTC 10 Jul 1987, as calculated by the model in the Na5 simulation.

caused by a geographical inhomogeneity of aerosol loading. In this subsection we further study the dependence of the various cloud microphysical states appearing in the correlation statistics on environmental factors, following the method of Brenguier et al. (2000) and Suzuki et al. (2010a,b) by adopting the conceptual adiabatic growth model. By comparing the RE–COT patterns with isolines of N_c and W shown in Figs. 12, 16, and 17, we can study whether cloud particles grow through an adiabatic growth process (e.g., condensation) or nonadiabatic growth processes (e.g., collision–coalescence, sedimentation, and evaporation).

According to the adiabatic model, the cloud water content q (g m^{-3}) is assumed to linearly increase with height h as

$$q = \lambda h. \tag{7}$$

The volume-averaged particle radius r_v is then given by

$$r_v(h) = \left(\frac{3}{4\pi\rho_w}\frac{q}{N_c}\right)^{1/3} = A^{1/3}h^{1/3}N_c^{-1/3}, \tag{8}$$

where $A = 3\lambda/(4\pi\rho_w)$. Also, the effective radius is related to r_v as $r_e = k^{-1/3}r_v$ and thus given as

$$r_e(h) = A^{1/3}h^{1/3}k^{-1/3}N_c^{-1/3}. \tag{9}$$

The effective radius at cloud top ($h = H$) is determined as

$$r_e(H) = A^{1/3}H^{1/3}k^{-1/3}N_c^{-1/3}. \tag{10}$$

Vertical integration of Eqs. (7) and (9) over cloud layers of thickness H then leads to expressions for liquid water path and optical thickness:

$$W = \int_0^H q\,dh = \frac{1}{2}\lambda H^2, \tag{11}$$

$$\tau = \frac{Q_{\text{ext}}\pi}{\rho_w 4/3\pi}\int_0^H \frac{q}{r_e}dh = \frac{3}{5}Q_{\text{ext}}\pi A^{2/3}(kN_c)^{-1/3}H^{5/3}, \tag{12}$$

where Q_{ext} is the extinction coefficient factor. From Eqs. (10), (11), and (12), effective radii at the cloud top can be

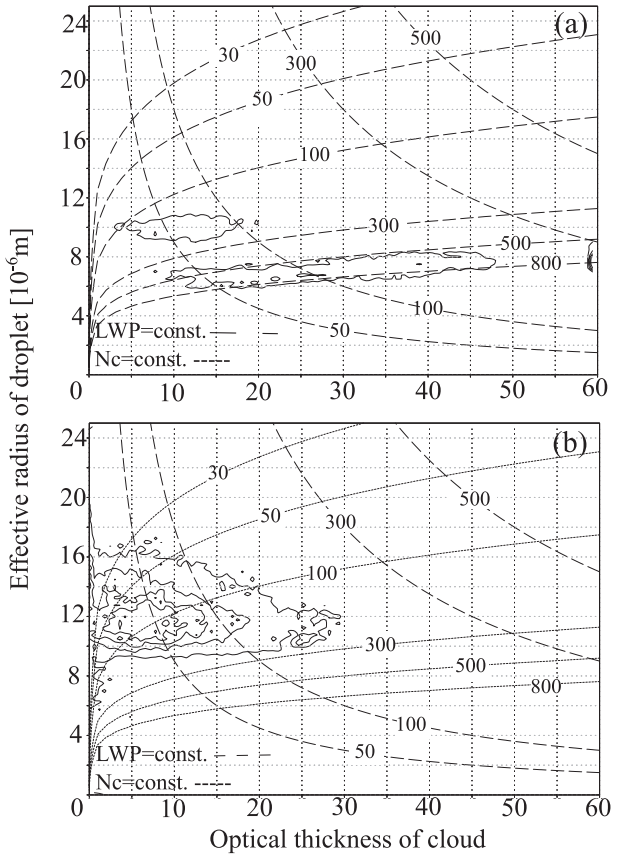

FIG. 19. Normalized correlation pattern of cloud optical thickness and cloud effective radius obtained from the results simulated from the Na3+W experiment, for the (a) northern and (b) southern parts of domain III. The contours are for 0.1, 0.3, 0.5, 0.7, and 0.9, with the maximum value set to 1.

obtained as expressed by Eq. (6). According to this model, τ and r_e are determined by the cloud-top height H, or equivalently by W, for a specified value of N_c. From Eq. (11) and the fact that the cloud-top height of all the sensitivity experiments conducted in section 3 was primarily determined by the inversion height assumed for each experiment, it can be argued that the inversion height controls W in each experiment, while N_c is not dependent on the inversion height. As a result, the RE–COT statistics for the sensitivity experiments of different inversion height tend to move across the isolines of W, whereas the plots for sensitivity experiments of changing aerosol amount under constant inversion height tend to move along the isolines of W, as summarized in Fig. 17.

We also estimated W differences from the inversion height sensitivity experiments to compare them with those obtained from the adiabatic theory. On the basis of Eq. (11), the W of the H0 (W_{0T}), H+300 (W_{300T}), and H+500 (W_{500T}) experiments were estimated to be 127, 260, and 374 g m^{-2}, respectively. The maximum values of W for each experiment (W_{0E}, W_{300E}, and W_{500E}) from Fig. 17 were about 120, 210, and 280 g m^{-2}, respectively. The differences between the theoretical and experimental values in H0, H+300, and H+500 were 7, 50, and 94 g m^{-2}, respectively. This means that cloud droplets in the H0 condition mainly grow through an adiabatic growth process (i.e., condensation growth was dominant), and that the higher the inversion height was, the more likely cloud droplets were to grow by nonadiabatic growth processes. An important example for such a nonadiabatic process is precipitation formation, and Fig. 11d shows that the rainfall amount was increasing with increasing inversion height. This result is consistent with the fact that the larger discrepancy of the cloud microphysical state from the adiabatic model as argued above.

5. Conclusions

Three-dimensional downscaling simulations using a spectral bin microphysics model were conducted to investigate effects of aerosols and dynamic stability of the atmosphere on the correlation statistics between the droplet radius and optical thickness of warm clouds over the FIRE region. JRA-25 and GTOPO30 data were used for the initial and boundary conditions of the numerical simulation, and the aerosol fields were also nested from the SPRINTARS global aerosol transport model simulation. The results showed that (i) the regeneration process of aerosols from evaporated cloud droplets is necessary to maintain the maritime stratocumulus in the model used in this study; (ii) the inversion height of the boundary layer changes the cloud liquid water path with small changes in the number concentration values; (iii) the number concentration of aerosols changes the number concentration of cloud droplets with small changes in the liquid water path values; (iv) the statistics between COT and RE consist of a mixture of positive and negative correlation patterns over air mass conditions with different aerosol amounts, similar to the satellite observation study of NN95; (v) a high inversion height makes cloud particles grow more by nonadiabatic growth processes; and (vi) most of the RE–COT statistics simulated in this study are accompanied by a ''high-heeled'' correlation pattern. Conclusions (ii) and (iii) confirm the results of previous modeling studies (e.g., Suzuki et al. 2010a), while trend (vi) was observed in the previous study only when the aerosol size spectrum was assumed to have a large negative slope. Conclusion (v) will require further analysis in future research for more detailed understanding of how nonadiabatic processes such as collision–coalescence and evaporation relate to the cloud life cycle and precipitation formation.

Acknowledgments. This study is supported by Initiative on Promotion of Supercomputing for Young Researchers, Supercomputing Division, Information Technology Center, The University of Tokyo. A part of authors are supported by projects of JAXA/GCOM-C, JAXA/EarthCARE, MEXT/VL for Climate System Diagnostics, MOE/Global Environment Research Fund A-1101, NIES/GOSAT, and MEXT/RECCA/SALSA. Some authors are supported by Grant-in-Aid for JSPS Fellows 22-7893. One of the authors is supported by the Korea Meteorological Administration Research and Development Program under Grant RACS 2010-1009. We are very grateful to Jørgen. B. Jensen of the National Center for Atmospheric Research/Earth Observation Factory for his valuable comment on an earlier version of this paper.

REFERENCES

Ackermann, A. S., and Coauthors, 2009: Large-eddy simulations of a drizzling, stratocumulus-topped marine boundary layer. *Mon. Wea. Rev.,* **137,** 1083–1110.

Albrecht, B. A., 1989: Aerosols, cloud microphysics, and fractional cloudiness. *Science,* **245,** 1227–1230.

——, D. A. Randall, and S. Nicholls, 1988: Observations of marine stratocumulus clouds during FIRE. *Bull. Amer. Meteor. Soc.,* **69,** 618–626.

——, C. S. Bretherton, D. Johnson, W. H. Scubert, and A. S. Frisch, 1995: The Atlantic Stratocumulus Transition Experiment—ASTEX. *Bull. Amer. Meteor. Soc.,* **76,** 889–904.

Asano, S., M. Shiobara, and A. Uchiyama, 1995: Estimation of cloud physical parameters from airborne solar spectral reflectance measurements for stratocumulus clouds. *J. Atmos. Sci.,* **52,** 3556–3576.

Bores, R., and L. D. Rotstayn, 2001: Possible links between cloud optical depth and effective radius in remote sensing observations. *Quart. J. Roy. Meteor. Soc.,* **127,** 2367–2383.

Brenguier, J.-L., H. Pawlowska, L. Schüller, R. Preusker, J. Fischer, and Y. Fouquart, 2000: Radiative properties of boundary layer clouds: Droplet effective radius versus number concentration. *J. Atmos. Sci.,* **57,** 803–821.

——, ——, and ——, 2003: Cloud microphysical and radiative properties for parameterization and satellite monitoring of the indirect effect of aerosol on climate. *J. Geophys. Res.,* **108,** 8632, doi:10.1029/2002JD002682.

Breon, F.-M., D. Tanré, and S. Generoso, 2003: Aerosol effect on cloud droplet size monitored from satellite. *Science,* **295,** 834–838.

Choi, I.-J., T. Iguchi, S.-W. Kim, S.-C. Yooh, and T. Nakajima, 2010: Simulation of aerosol effect on the microphysical properties of shallow stratocumulus cloud over East Asia using a bin-based meso-scale cloud model. *Atmos. Chem. Phys. Discuss.,* **10,** 23 449–23 495.

Feingold, G., S. M. Kreidenweis, B. Stevens, and W. R. Cotton, 1996: Numerical simulations of stratocumulus processing of cloud condensation nuclei through collision-coalescence. *J. Geophys. Res.,* **101** (D16), 21 391–21 402.

——, I. Koren, H. Wang, H. Xue, and W. A. Brewer, 2010: Precipitation-generated oscillations in open cellular cloud fields. *Nature,* **466,** 849–852, doi:10.1038/nature09314.

Han, Q., W. B. Rossow, and A. A. Lacis, 1994: Near-global survey of effective droplet radii in liquid water clouds using ISCCP data. *J. Climate,* **7,** 465–497.

——, ——, J. Chou, and R. M. Welch, 1998: Global survey of the relationships of cloud albedo and liquid water path with droplet size using ISCCP. *J. Climate,* **11,** 1516–1528.

Iguchi, T., T. Nakajima, A. P. Khain, K. Saito, T. Takemura, and K. Suzuki, 2008: Modeling the influence of aerosols on cloud microphysical properties in the East Asia region using a meso-scale model coupled with a bin-based cloud microphysics scheme. *J. Geophys. Res.,* **113,** D14215, doi:10.1029/2007JD009774.

Ikawa, M., and K. Saito, 1991: Description of a non-hydrostatic model developed at the forecast research department of MRI. Meteorological Research Institute Tech. Rep. 28, 238 pp.

Ivanova, I. T., and H. G. Leighton, 2008: Aerosol–cloud interactions in a mesoscale model. Part II: Sensitivity to aqueous-phase chemistry. *J. Atmos. Sci.,* **65,** 309–330.

Kawamoto, K., T. Nakajima, and T. Y. Nakajima, 2001: A global determination of cloud microphysics with AVHRR remote sensing. *J. Climate,* **14,** 2045–2068.

Khain, A. P., M. Ovtchinnikov, M. Pinsky, A. Pokrovsky, and H. Krugliak, 2000: Notes on the state-of-the-art numerical modeling of cloud microphysics. *Atmos. Res.,* **55,** 159–224.

——, D. Rosenfeld, and A. Pokrovsky, 2005: Aerosol impact on the dynamics and microphysics of deep convective clouds. *Quart. J. Roy. Meteor. Soc.,* **131,** 2639–2663, doi:10.1256/qj.04.62.

Klein, S., and D. L. Hartmann, 1993: The seasonal cycle of low stratiform cloud. *J. Climate,* **6,** 1587–1606.

Kobayashi, T., and K. Masuda, 2008: Effects of precipitation on the relationships between cloud optical thickness and drop size derived from space-borne measurements. *Geophys. Res. Lett.,* **35,** L24809, doi:10.1029/2008GL036140.

Lebsock, M. D., G. L. Stephens, and C. Kummerow, 2008: Multi-sensor satellite observations of aerosol effects on warm clouds. *J. Geophys. Res.,* **113,** D15205, doi:10.1029/2008JD009876.

Lin, Y.-L., R. D. Farley, and H. D. Orville, 1983: Bulk parameterization of the snow field in a cloud model. *J. Climate Appl. Meteor.,* **22,** 1065–1092.

Lohmann, U., G. Tselioudis, and C. Tyler, 2000: Why is the cloud albedo–particle size relationship different in optically thick and optically thin clouds? *Geophys. Res. Lett.,* **27,** 1099–1102.

Masunaga, H., T. Y. Nakajima, T. Nakajima, M. Kachi, and K. Suzuki, 2002: Physical properties of maritime low clouds as retrieved by combined use of Tropical Rainfall Measurement Mission (TRMM) Microwave Imager and Visible/Infrared Scanner. 2. Climatology of warm clouds and rain. *J. Geophys. Res.,* **107,** 4367, doi:10.1029/2001JD001269.

Matsui, T., H. Masunaga, and R. A. Pielke Sr., 2004: Impact of aerosols and atmospheric thermodynamics on cloud properties within the climate system. *Geophys. Res. Lett.,* **31,** L06109, doi:10.1029/2003GL019287.

McCaa, J. R., and C. S. Bretherton, 2004: A new parameterization for shallow cumulus convection and its application to marine subtropical cloud-topped boundary layers. Part II: Regional simulations of marine boundary layer clouds. *Mon. Wea. Rev.,* **132,** 883–896.

Mechem, D. B., and Y. L. Kogan, 2003: Simulating the transition from drizzling marine stratocumulus to boundary layer cumulus with a mesoscale model. *Mon. Wea. Rev.,* **131,** 2342–2360.

——, P. C. Robinson, and Y. L. Kogan, 2006: Processing of cloud condensation nuclei by collision–coalescence in a mesoscale model. *J. Geophys. Res.,* **111,** D18204, doi:10.1029/2006JD007183.

Mitra, S. K., J. Brinkmann, and H. R. Pruppacher, 1992: A wind tunnel study on the drop-to-particle conversion. *J. Aerosol Sci.,* **23,** 245–256.

Mocko, D. M., and W. R. Cotton, 1995: Evaluation of fractional cloudiness parameterizations for use in mesoscale model. *J. Atmos. Sci.,* **52,** 2884–2901.

Myhre, G., and Coauthors, 2007: Aerosol–cloud interaction inferred from MODIS satellite data and global aerosol models. *Atmos. Chem. Phys.,* **7,** 3081–3101.

Nakajima, T., and M. D. King, 1990: Determination of the optical thickness and effective particle radius of clouds from reflected solar radiation measurements. Part I: Theory. *J. Atmos. Sci.,* **47,** 1878–1893.

——, ——, J. D. Spinhirne, and L. F. Radke, 1991: Determination of the optical thickness and effective particle radius of clouds from reflected solar radiation measurements. Part II: Marine stratocumulus observations. *J. Atmos. Sci.,* **48,** 728–751.

——, M. Tsukamoto, Y. Tsushima, A. Numaguti, and T. Kimura, 2000: Modeling of the radiative process in an atmospheric general circulation model. *Appl. Opt.,* **39,** 4869–4878.

——, A. Higurashi, K. Kawamoto, and J. E. Penner, 2001: A possible correlation between satellite-derived cloud and aerosol microphysical parameters. *Geophys. Res. Lett.,* **28,** 1171–1174.

Nakajima, T. Y., and T. Nakajima, 1995: Wide-area determination of cloud microphysical properties from NOAA AVHRR measurements for FIRE and ASTEX regions. *J. Atmos. Sci.,* **52,** 4043–4059.

Onogi, K., and Coauthors, 2007: The JRA-25 reanalysis. *J. Meteor. Soc. Japan,* **85,** 369–432.

Quaas, J., O. Boucher, N. Bellouin, and S. Kinne, 2008: Satellite-based estimate of the direct and indirect aerosol climate forcing. *J. Geophys. Res.,* **113,** D05204, doi:10.1029/2007JD008962.

Rogers, R. R., and M. K. Yau, 1989: *A Short Course in Cloud Physics*. 3rd ed. Pergamon Press, 293 pp.

Saito, K., and Coauthors, 2006: The operational JMA nonhydrostatic mesoscale model. *Mon. Wea. Rev.,* **134,** 1266–1298.

Sato, Y., T. Nakajima, K. Suzuki, and T. Iguchi, 2009: Application of a Monte Carlo integration method to collision and coagulation growth processes of hydrometeors in a bin-type model. *J. Geophys. Res.,* **114,** D09215, doi:10.1029/2008JD011247.

Savic-Jovcic, V., and B. Stevens, 2008: The structure of mesoscale organization of precipitating stratocumulus. *J. Atmos. Sci.,* **65,** 1587–1605.

Sekiguchi, M., and T. Nakajima, 2008: A *k*-distribution-based radiation code and its computational optimization for an atmospheric general circulation model. *J. Quant. Spectrosc. Radiat. Transfer,* **109,** 2779–2793.

——, ——, K. Suzuki, K. Kawamoto, A. Higurashi, D. Rosenfeld, I. Sano, and S. Mukai, 2003: A study of the direct and indirect effects of aerosols using global satellite datasets of aerosol and cloud parameters. *J. Geophys. Res.,* **108,** 4699, doi:10.1029/2002JD003359.

Stephens, G. L., 2005: Cloud feedbacks in the climate system: A critical review. *J. Climate,* **18,** 237–273.

Stevens, B., and Coauthors, 2003: Dynamics and Chemistry of Marine Stratocumulus—DYCOMS-II. *Bull. Amer. Meteor. Soc.,* **84,** 579–593.

——, and Coauthors, 2005: Evaluation of large-eddy simulations via observations of nocturnal marine stratocumulus. *Mon. Wea. Rev.,* **133,** 1443–1462.

Suzuki, K., T. Nakajima, A. Numaguti, T. Takemura, K. Kawamoto, and A. Higurashi, 2004: A study of the aerosol effect on a cloud field with simultaneous use of GCM modeling and satellite observation. *J. Atmos. Sci.,* **61,** 179–194.

——, ——, T. Y. Nakajima, and A. P. Khain, 2006: Correlation pattern between effective radius and optical thickness of water clouds simulated by a spectral bin microphysics cloud model. *SOLA,* **2,** 116–119, doi:10.2151/sola.2006-030.

——, ——, ——, and ——, 2010a: A study of microphysical mechanisms for correlation patterns between droplet radius and optical thickness of warm clouds with a spectral bin microphysics model. *J. Atmos. Sci.,* **67,** 1126–1141.

——, ——, ——, and G. L. Stephens, 2010b: Effect of the droplet activation process on microphysical properties of warm clouds. *Environ. Res. Lett.,* **5,** 024012, doi:10.1088/1748-9326/5/2/024012.

Takemura, T., T. Nozawa, S. Emori, T. Y. Nakajima, and T. Nakajima, 2005: Simulation of climate response to aerosol direct and indirect effects with aerosol transport-radiation model. *J. Geophys. Res.,* **110,** D02202, doi:10.1029/2004JD005029.

Tao, W.-K., X. Li, A. Khain, T. Matsui, S. Lang, and J. Simpson, 2007: Role of atmospheric aerosol concentration on deep convective precipitation: Cloud-resolving model simulations. *J. Geophys. Res.,* **112,** D24S18, doi:10.1029/2007JD008728.

Twomey, S., 1974: Pollution and the planetary albedo. *Atmos. Environ.,* **8,** 1251–1256.

Wang, H., and G. Feingold, 2009a: Modeling mesoscale cellular structures and drizzle in marine stratocumulus. Part I: Impact of drizzle on the formation and evolution of open cells. *J. Atmos. Sci.,* **66,** 3237–3256.

——, and ——, 2009b: Modeling mesoscale cellular structures and drizzle in marine stratocumulus. Part II: The microphysics and dynamics of the boundary region between open and closed cells. *J. Atmos. Sci.,* **66,** 3257–3275.

——, ——, R. Wood, and J. Kazil, 2010: Modelling microphysical and meteorological controls on precipitation and cloud cellular structures in southeast Pacific stratocumulus. *Atmos. Chem. Phys.,* **10,** 6347–6362.

——, P. J. Rasch, and G. Feingold, 2011: Manipulating marine stratocumulus cloud amount and albedo: A process-modeling study of aerosol–cloud–precipitation interactions in response to injection of cloud condensation nuclei. *Atmos. Chem. Phys.,* **11,** 4237–4249.

Wang, S., B. A. Albrecht, and P. Minnis, 1993: A regional simulation of marine boundary-layer clouds. *J. Atmos. Sci.,* **50,** 4022–4043.

Xue, H., G. Feingold, and B. Stevens, 2008: Aerosol effects on clouds, precipitation, and the organization of shallow cumulus convection. *J. Atmos. Sci.,* **65,** 392–406.

Yamada, Y., 2003: Cloud microphysics (in Japanese). The JMA non-hydrostatic model, JMA Annual Rep. 49, 52–76.